IOP Publishing Journal of Physics: Condensed Matter
J. Phys.: Condens. Matter **32** (2020) 184001 (12pp) https://doi.org/10.1088/1361-648X/ab699e

Pyrene-stabilized acenes as intermolecular singlet fission candidates: importance of exciton wave-function convergence

Xingyu Liu[1], Rithwik Tom[2], Xiaopeng Wang[1,3], Cameron Cook[4], Bohdan Schatschneider[4] and Noa Marom[1,2,5,6]

[1] Department of Materials Science and Engineering, Carnegie Mellon University, Pittsburgh, PA, United States of America
[2] Department of Physics, Carnegie Mellon University, Pittsburgh, PA, United States of America
[3] Qingdao Institute for Theoretical and Computational Science, Shandong University, Qingdao, Shandong 266237, People's Republic of China
[4] Department of Chemistry and Biochemistry, California State Polytechnic University at Pomona, Pomona, CA, United States of America
[5] Department of Chemistry, Carnegie Mellon University, Pittsburgh, PA, United States of America

E-mail: nmarom@andrew.cmu.edu

Received 7 October 2019, revised 3 December 2019
Accepted for publication 9 January 2020
Published 4 February 2020

Abstract

Singlet fission (SF) is a photophysical process considered as a possible scheme to bypass the Shockley–Queisser limit by generating two triplet-state excitons from one high-energy photon. Polyacene crystals, such as tetracene and pentacene, have shown outstanding SF performance both theoretically and experimentally. However, their instability prevents them from being utilized in SF-based photovoltaic devices. In search of practical SF chromophores, we use many-body perturbation theory within the GW approximation and Bethe–Salpeter equation to study the excitonic properties of a family of pyrene-stabilized acenes. We propose a criterion to define the convergence of exciton wave-functions with respect to the fine **k**-point grid used in the BerkeleyGW code. An open-source Python code is presented to perform exciton wave-function convergence checks and streamline the double Bader analysis of exciton character. We find that the singlet excitons in pyrene-stabilized acenes have a higher degree of charge transfer character than in the corresponding acenes. The pyrene-fused tetracene and pentacene derivatives exhibit comparable excitation energies to their corresponding acenes, making them potential SF candidates. The pyrene-stabilized anthracene derivative is considered as a possible candidate for triplet–triplet annihilation because it yields a lower SF driving force than anthracene.

Keywords: molecular crystals, singlet fission, electronic structure, GW+BSE, excitons

S Supplementary material for this article is available online

(Some figures may appear in colour only in the online journal)

1. Introduction

Intermolecular singlet exciton fission (SF) is a photophysical process where one singlet exciton (S_1) is converted into two triplet excitons (T_1) residing on two neighboring organic chromophores [1–6]. Because of its potential to circumvent the single-junction Shockley–Queisser limit [7, 8], SF has gained wide attention. Various strategies of pairing SF materials with a low-gap complementary semiconductor to build a SF-based photovoltaic (PV) device have been attempted [9–20]. Ehrler

[6] Author to whom any correspondence should be addressed.

et al built a hybrid SF solar cell device using crystalline pentacene as the SF material and lead chalcogenide quantum dots for triplet harvesting, which achieved a total power conversion efficiency (PCE) of 4.7% [11]. Einzinger *et al* paired crystalline silicon with crystalline tetracene as the SF material, as suggested by Dexter in 1979 [21], resulting in a total PCE of 5.1% [17]. Congreve *et al* implemented devices based on triplet exciton transfer from pentacene to C_{60} [9]. Additional ideas, such as utilizing SF materials for photon multiplication or building a double-terminal SF tandem system have also been proposed [4, 16]. In any design strategy, in order to maximize the PCE the SF chromophore is expected to generate triplet excitons with energies matching the optical bandgap of the complementary semiconductor layer [1, 4, 7, 17, 21]. However, known classes of SF materials have largely failed to provide a combination of good SF performance, in terms of fast fission and high quantum yield, photostability, and compatibility with commonly used semiconductors [3, 4, 22]. Despite recent progress in the understanding of intramolecular SF [23–26], some key aspects of the intermolecular SF mechanism remain unclear [27–30]. This hinders the design and discovery of new materials for intermolecular SF. Thus, solid-state SF-based PV technology has hitherto remained in the incubation stage. The dearth of SF materials calls for searching previously unexplored classes of chromophores for potential SF candidates.

Several criteria have been identified for material characteristics likely to result in good intermolecular SF performance. The primary criterion is thermodynamically favorable conversion from S_1 to $2T_1$, which would lead to almost unidirectional fission with a high rate [20, 31, 32]. However, excess exothermicity of the SF process would cause losses in solar energy conversion [7]. Hence, materials with nearly degenerate singlet and triplet-pair energy levels ($E_S - 2E_T \approx 0$) may be preferable [10, 21]. Most crystalline organic semiconductors do not meet this requirement. A secondary criterion is a singlet exciton with charge transfer (CT) character, where the electron probability distribution is centered on different molecules than the hole [3, 33–38]. It has been argued that within the indirect SF mechanism picture, the CT percentage of the lowest-lying S_1 is positively correlated with the coupling between S_1 and multiexciton states, which influences SF dynamics [3, 39–41]. In molecular crystals, the packing motif may alter both the thermodynamic driving force for SF and the singlet exciton character, and thus play an important role in SF performance [4, 42–44]. It has been suggested that slip-stacked packing could be an optimal configuration for some classes of materials [2, 36, 44]. However, no consensus has been reached on this topic. Among the experimentally corroborated SF chromophores, polyacenes such as tetracene, pentacene, and some of their derivatives remain ahead in the race for SF performance. Pentacene has been observed to undergo rapid SF with a 200% triplet yield [6, 45, 46]. This has stimulated extensive research of pentacene-based PV devices. However, the experimental $E_S - 2E_T$ for crystalline pentacene is about 0.13 eV [45, 47–49]. This non-negligible exothermicity may lead to a considerable energy loss in a solar cell. In comparison, the experimental $E_S - 2E_T$ of crystalline tetracene is −0.12 eV. While this may be advantageous for reducing energy losses, it leads to a slower fission rate and lower quantum yield than in pentacene [48–51].

Although both tetracene and pentacene have been used in SF-based PV devices, their feasibility of operating as light-absorbing layers in commercial modules is still questionable. A major issue is their stability. Crystalline polyacenes, especially larger acene molecules are photosensitive. Acene crystals may degrade after a few hundred hours of illumination even when encapsulated in glass [4]. Moreover, dimerization and oxidation of acene molecules may be induced by solvation in organic solvents and exposure to air, respectively. Another shortcoming is the poor solubility of longer acene molecules, which makes their processing challenging [52]. These flaws demand design strategies to increase the stability and solubility of longer acenes, and simplify their synthesis, without detracting from their outstanding SF performance.

A prevalent strategy for stabilizing acene molecules is functionalizing their peripheral sites with bulky electron-withdrawing moieties [52]. Some of these stabilized acene derivatives have been investigated in the context of SF. 6,13-bis(trii sopropylsilylethynyl) pentacene (TIPS-pentacene), and its tetracene counterpart 6,11-bis-(triisopropylsilylethynyl)-tetracene (TIPS-tetracene), were originally developed for applications in organic field-effect transistors (OFET) and organic light-emitting diodes (OLED). Both have been found to undergo SF and have been used in PV devices [18, 38]. Outstanding charge mobility combined with enhanced stability and solubility makes these two chromophores promising alternatives to pentacene and tetracene as light-absorbing materials. Phenylation is another method of stabilizing large acene molecules while preserving their optical properties. Phenylated acenes have been studied theoretically and experimentally in the gas phase and in the solid state. SF has been observed in 5,12-diphenyltetracene (DPT), rubrene, and 6,13-diphenylpentacene (DPP) [32, 53–57] and theoretically predicted to occur in crystalline quaterrlyene, 6-phenylpentacene (MPP), 5,7,12,14-tetraphenyl-pentacene (TPP), 1,4,6,8,11,13-hexaphenyl-pentacene (HPP), 1,2,3,4,6,8,9,10,11,13-decaphenyl-pentacene (DcPP), triclinic and monoclinic rubrene, and TIPS-anthracene [35, 36, 43, 58]. Enhanced photooxidative resistance and stability have also been observed in some nitrogen-substituted acene (azaacene) derivatives, whose $E_S - 2E_T$ could be tuned by modifying the number of nitrogen atoms and the substitution sites [52, 59].

Recently, a family of stabilized pyrene-fused acenes (PFA) have been synthesized and crystallized in the context of OFETs and OLEDs [60–63]. PFAs have smaller gaps between the highest occupied molecular orbital (HOMO) and lowest unoccupied molecular orbital (LUMO) compared to the corresponding acene molecules [60, 61]. PFA crystals can remain stable in air for longer than five days without any protective coating [60–63]. Additionally, PFA molecules exhibit enhanced solubility in common solvents such as methylene chloride, chloroform, tetrahydrofuran and *N*,*N*-dimethylformamide. These properties could make PFAs attractive candidates for the realization of practical SF-based PV devices. Here, PFAs are studied in the context of SF for the first time.

Figure 1 shows the single molecule and crystal structures of anthracene (ANT), tetracene (TET), pentacene (PEN) and hexacene (HEX), and four PFAs, tetrabenzo [*de*,*no*,*st*,c_1d_1]-heptacene(TBHA),5,7,14,16-tetraphenyl-8:9,12:13-bis-benzo-hexatwistacene (TBH), 1,2,3,4,6,8,15,17- octaphenyl-9:10,13:14-bisbenzoheptatwistacene (OBH), and 6,8,10,17,19,21-hexa-phenyl-1.22,4.5,11.12,15.16-tetrabenzo-nonatwistacene (HTN), with their Cambridge Structural Database (CSD) reference codes ANTCEN [64], TETCEN01 [65], PENCEN [66], ZZZDKE01 [67], TBZHCE [68], CARREU [60], TAYSUJ [62], and KECLAH [61]. The typical herringbone (HB) packing [49, 69] of polyacene crystals is shown in figures 1(a)–(d). TBHA, with no side groups except for the pyrene terminals, displays co-facial π-stacking along the *a* axis (Hirshfeld surface analysis shows that ~28% of the intermolecular close contact fractions are associated with C···C contacts—see supporting information). For PFAs with additional phenyl side groups, steric barriers reduce the co-facial interactions to the extent that the Hirshfeld intermolecular close contact fractions associated with C···C contacts is less than or equal to 5.0% (see supporting information). TBH and OBH, with a single pyrene terminal and several phenyl side groups, exhibit π-stacking of the pyrene terminals, while their acene backbones have very little co-facial interactions (See the deconvoluted Hirshfeld surfaces in the supporting information) [62]. HTN, with two pyrene terminals and six phenyl side groups, presents slip stacking of the acene backbones along the *c* axis and weak π–π stacking between neighboring pyrene terminals along the *a* axis. In addition to altering the crystal packing, the phenyl side groups in PFAs cause backbone twisting, which is believed to contribute to the enhanced stability of PFAs compared to polyacene crystals (See the deconvoluted Hirshfeld surfaces in the supporting information) [63].

To investigate the potential of PFAs as SF materials, we conduct many-body perturbation theory calculations, employing the GW approximation and the Bethe–Salpeter equation (BSE). The double-Bader analysis (DBA) method [35] is used to evaluate the degree of exciton CT character. The DBA procedure is streamlined by the new open-source Python library, dbaAutomator. Unconverged exciton wave-functions (EWF) may introduce artifacts in DBA, therefore a detailed technical discussion of EWF convergence is provided in the Methods section. The optical properties of PFAs are studied in both the gas phase and solid state, and systematically compared with acenes to elucidate the effect of the pyrene terminals. We find that the pyrene-fused anthracene derivative, TBHA, could be a prospective candidate for triplet–triplet annihilation (TTA). The pyrene-fused tetracene and pentacene derivatives TBH, OBH, and HTN could be prospective SF candidates with enhanced stability.

2. Methods

2.1. Geometry optimization

The starting geometries of crystalline PFAs and polyacenes were obtained from the CSD. Single molecule geometries were optimized using density functional theory (DFT) with the generalized gradient approximation of Perdew, Burke and Ernzerhof (PBE) [70] coupled to the Tkatchenko–Scheffler (TS) [71] pairwise dispersion method, implemented in the FHI-aims [72–74] electronic structure package. Optimization of crystal structures was performed with the CASTEP [75] code using PBE + TS. Norm-conserving pseudopotentials were utilized for C and H atoms. The plane-wave basis set cutoff was 750 eV and the Monkhorst–Pack **k**-point grid spacing was 0.07 Å^{-1}. The convergence criteria for the total energy, maximum force, maximum stress, and maximum displacement were 5×10^{-6} eV/atom, 0.01 eV Å^{-1}, 0.02 GPa, and 5×10^{-4} Å^{-1}, respectively.

2.2. GW approximation and Bethe–Salpeter equation

Single molecule quaisiparticle (QP) energies and optical properties were calculated with the GW approximation and the Bethe–Salpeter equation (GW+BSE) using FHI-aims with *aug2tier2* basis sets [76]. The PBE exchange-correlation functional was chosen as the mean-field starting point for the non-self-consistent G_0W_0 calculation. Previous benchmarks have shown that this is a sufficiently accurate starting point for polycyclic aromatic hydrocarbons (PAHs) [77]. The optical properties were subsequently calculated by solving the BSE within the Tamm–Dancoff approximation (TDA) [78, 79]. It has been shown that TDA is effective in overcoming triplet instabilities while introducing insignificant errors to the lowest excited-state energies of gas-phase molecules [80]. 30 occupied states and 30 unoccupied states were considered in the BSE calculation. We note that the effect of molecular vibrations [81, 82] is not considered here.

GW+BSE calculations for crystalline PFAs and polyacenes were conducted with the BerkeleyGW package [79, 83, 84]. The convergence of numerical settings for crystalline PAHs has been discussed previously [43]. The prerequisite DFT eigenvectors and eigenfunctions with both coarse and fine **k**-point grids were generated with the Quantum Espresso [85] package using the PBE exchange-correlation functional and Troullier–Martins norm-conserving pseudopotentials [86]. The kinetic energy cutoff for wave-functions was set to 50 Ry. The polarizability, inverse dielectric matrices, and GW self-energy operator were constructed based on the mean-field eigenvalues and eigenfunctions using coarse **k**-point settings. Around 550 unoccupied bands were included in constructing the dielectric function and self-energy operator. The static remainder correction was applied to accelerate the convergence with respect to the number of unoccupied states [87].

Optical properties, including excitation energies, EWFs, and absorption spectra were calculated by solving the BSE within the TDA. 24 valence bands and 24 conduction bands were included in the calculation. Taking the full dielectric matrix as input to screen the attraction between the electron (***e***) and hole (***h***), the ***e***–***h*** interaction kernel was constructed on a coarse **k**-point grid. To construct the Bethe–Salpeter Hamiltonian, the QP energies and ***e***–***h*** interaction kernel calculated with coarse **k**-point settings were interpolated onto a

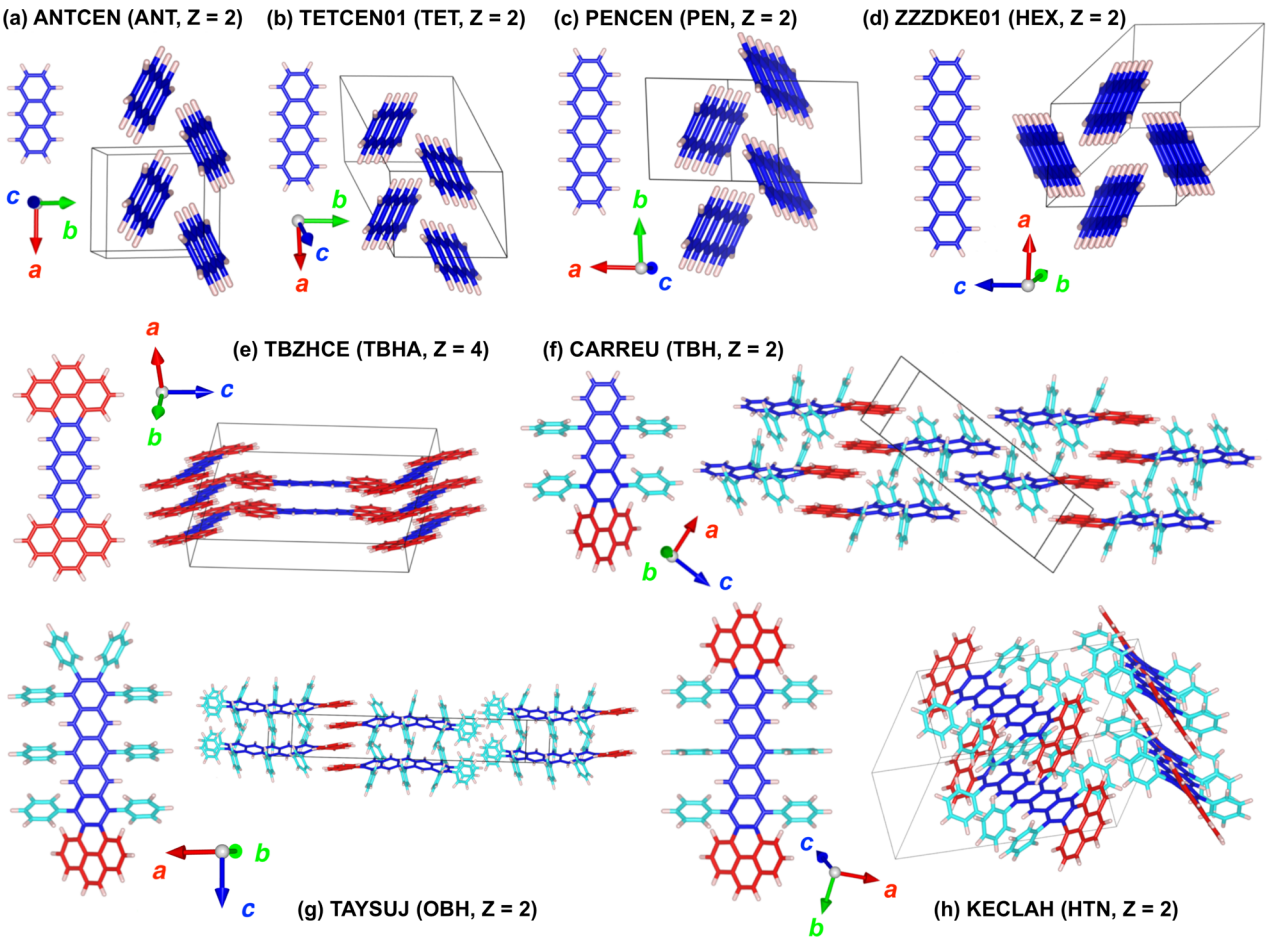

Figure 1. Illustration for single molecule and crystal structures of four polyacenes: anthracene, tetracene, pentacene, and hexacene, and four PFAs. The acene backbones are colored in dark blue, the pyrene terminals are colored in red, and the phenyl side groups are colored in light blue. The corresponding CSD reference codes from (a) to (h) are: ANTCEN [64], TETCEN01 [65], PENCEN [66], ZZZDKE01 [67], TBZHCE [68], CARREU [60], TAYSUJ [62], KECLAH [61]. The corresponding abbreviations and the number of molecule per cell (Z) are shown in parentheses after each reference code.

fine **k**-point grid. The subsequent diagonalization yielded the excitation energies and wave-functions [79]. The supercell size for the EWF calculation is consistent with the fine grid settings. The coarse grids and densest fine grids used for crystalline PFAs and polyacenes are listed in table 1. Convergence tests with respect to the number of unoccupied bands in the GW approximation and the number of valence and conduction bands included in the BSE calculation are provided in the supporting information (stacks.iop.org/JPhysCM/32/184001/mmedia) for anthracene, as a representative example. The fine grid convergence for EWF calculations is discussed in detail in section 2.3 below.

Table 1. The coarse and fine k-grid settings used here for crystalline PFAs and polyacenes.

CSD identifier	Coarse **k**-grid	Fine **k**-grid
ANTCEN	$4 \times 4 \times 2$	$8 \times 8 \times 6$
TETCEN01	$4 \times 4 \times 2$	$8 \times 8 \times 4$
PENCEN	$4 \times 4 \times 2$	$8 \times 8 \times 4$
ZZZDKE01	$4 \times 2 \times 4$	$10 \times 4 \times 10$
TBZHCE	$8 \times 1 \times 1$	$24 \times 4 \times 4$
CARREU	$4 \times 4 \times 1$	$8 \times 8 \times 6$
TAYSUJ	$1 \times 2 \times 4$	$4 \times 8 \times 12$
KECLAH	$4 \times 1 \times 2$	$10 \times 6 \times 8$

2.3. Convergence of EWF

EWF calculations are central to predicting and interpreting the excitonic properties of materials. The EWF provides important information on the exciton distribution and character (Frenkel versus CT) [33, 35]. Therefore, we provide a detailed technical discussion of EWF convergence with the BerkeleyGW package [79]. If the supercell for the EWF calculation, which corresponds to the fine **k**-point grid, is not sufficiently large, the electron density may be spuriously delocalized and spread across the supercell boundary. Therefore, a measure of convergence is to ensure that the EWF is fully contained within the supercell with minimal density close to the edges.

An example for TBHA is shown in figure 2. The EWF is visualized in the *bc* and *ac* planes with an isosurface value of 1.8×10^{-6} a.u. after normalization. The hole position is indicated by a red dot and the electron charge distribution is shown in yellow. With fine **k**-point grids of $16 \times 2 \times 2$ and $20 \times 2 \times 2$, the electron density distributes along the *a* axis, which corresponds to the π-stacking direction, and significant

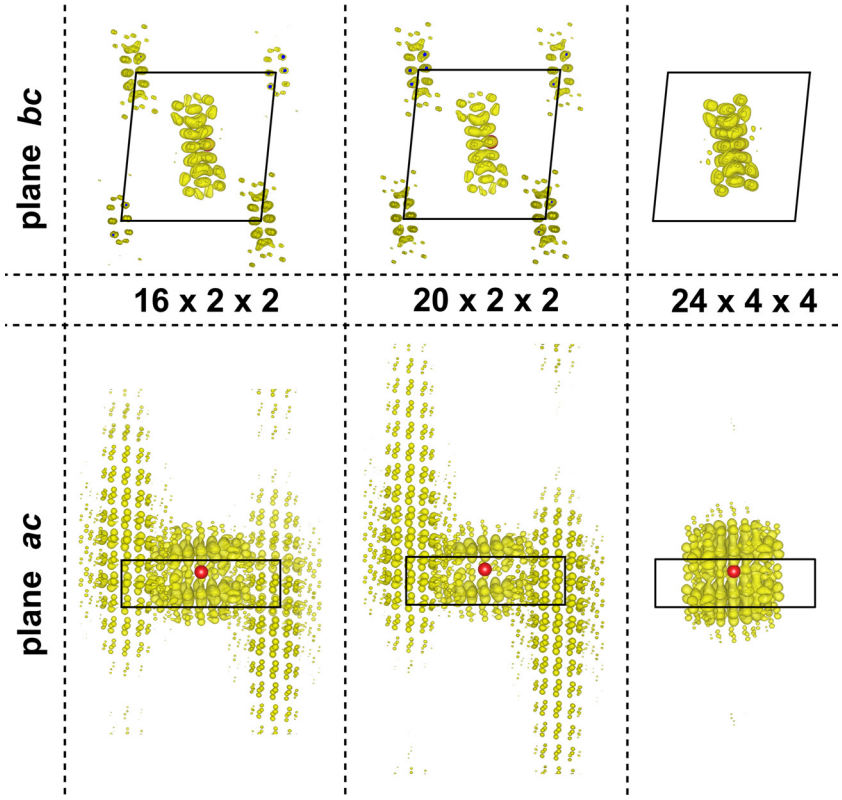

Figure 2. Visualization of the singlet state EWFs of TBHA with different supercell sizes. The EWF is viewed in the *bc* and *ac* planes. The hole position is indicated by a red dot the electron charge distribution is shown in yellow. All EWFs were plotted with an isosurface value of 1.8×10^{-6} a.u. after normalization. The central unit cell is indicated by a black box. Atoms are not shown for clarity. For unconverged supercells of $16 \times 2 \times 2$ and $20 \times 2 \times 2$, significant electron density is observed close to the supercell edges. For a converged supercell of $24 \times 4 \times 4$, the EWF is contained in the central region.

electron density is seen in the region close to the supercell edge. When the supercell size is increased to $24 \times 4 \times 4$, the electron density is fully contained in the central region of the supercell with no artifacts. Visualizations of the EWFs in reciprocal space, provided in figure S3 in the supporting information, also show that the EWF is not yet converged with fine grids of $16 \times 2 \times 2$ and $20 \times 2 \times 2$. As a consequence, the CT character determined by DBA is sensitive to the supercell size. CT character of 95.43%, 97.41%, and 94.38% is obtained with fine grids of $16 \times 2 \times 2$, $20 \times 2 \times 2$, and $24 \times 4 \times 4$, respectively. The lowest-lying singlet exciton energy (E_S) is not as sensitive to the fine **k**-point grid. The E_S values obtained for TBHA using $16 \times 2 \times 2$, $20 \times 2 \times 2$, and $24 \times 4 \times 4$ fine grids are 2.29 eV, 2.30 eV, and 2.28 eV, respectively. This indicates that the EWFs may still be distorted even though E_S is close to convergence with respect to the fine **k**-point grid. This may be attributed to the fact that in BerkeleyGW the real-space EWF is obtained by a discrete Fourier transform of the reciprocal-space EWF. This result emphasizes the importance of converging both the exciton energies and the EWFs.

To determine the converged supercell size for EWF calculations we follow a similar rationale to the approach proposed in [36] for determining the amount of vacuum required to converge single molecule calculations with BerkeleyGW. First, the hole position is fixed on a molecule in the central sub-cell. Second, the fraction of edge charge is evaluated by summing over the Bader charges on the atoms in the edge region and dividing by the total charge contained in the supercell. The edge distance, d, is defined as a fraction of the lattice parameters. The central region as a fraction of the total volume is then given by:

$$C = (1 - 2 \times d)^3. \quad (1)$$

In figure 3, the edge charge is plotted as a function of the edge distance, d, for varying supercell sizes. The edge distance is increased in increments of 5%. Based on equation (1), when d is 5% C is 72.9%, and when d is 45% C is only 0.1%. Hence, for a given supercell size, the edge charge increases sharply as the edge distance approaches 45%. The smallest supercells used here have a fine grid twice as dense as the coarse grid, as suggested by Sharifzadeh *et al* for pentacene [33]. As the supercell size increases the fraction of edge charge decreases for all systems studied here. For example, the EWF of HTN was calculated using four fine **k**-point grid settings, $8 \times 2 \times 4$, $8 \times 4 \times 6$, $8 \times 6 \times 6$, and $10 \times 6 \times 8$. The edge electron charge density percentage drops significantly when the supercell size is increased from $8 \times 2 \times 4$ to $8 \times 4 \times 6$. Another significant drop is observed with the supercell size increased to $10 \times 6 \times 8$.

As shown in figure 3, the EWF convergence behavior is system dependent. Acene crystals with herringbone packing, such as ANT and HEX, exhibit a different characteristic behavior than the PFA crystals. For crystals with π-stacking,

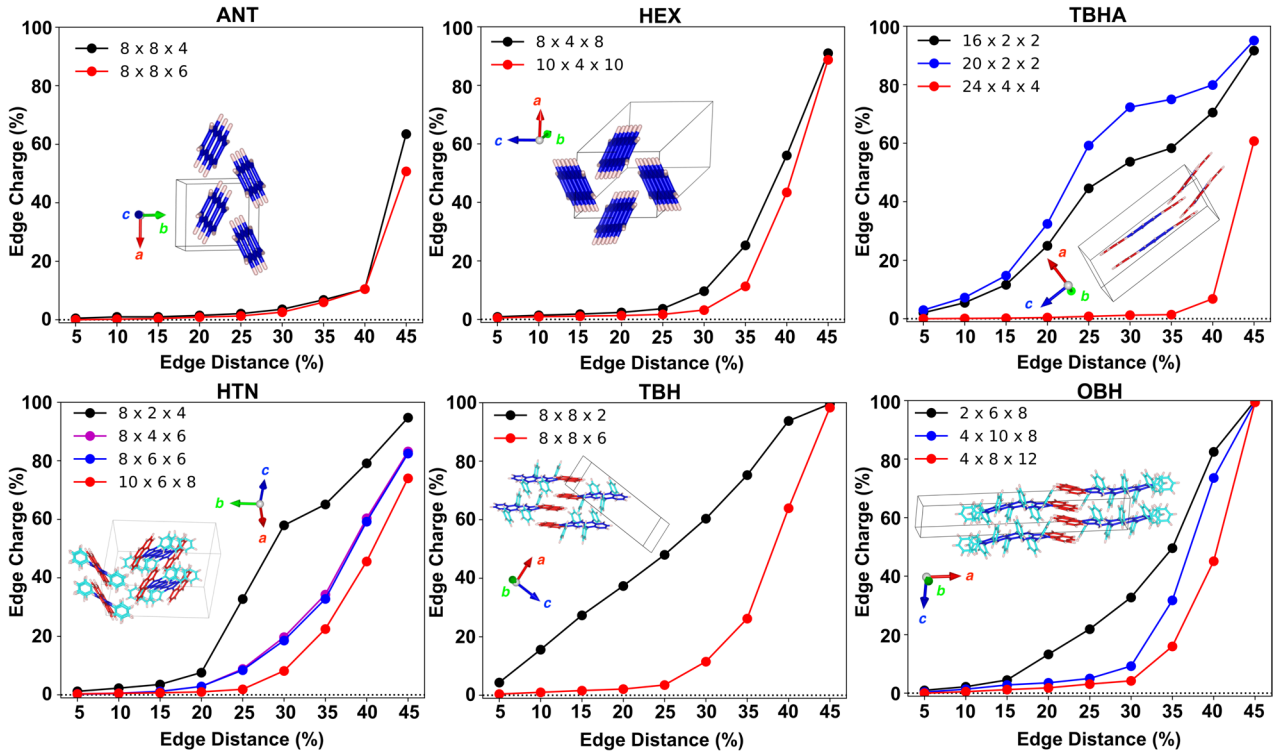

Figure 3. Edge charge as a function of edge distance with different supercell sizes for representative acenes and PFAs.

the EWF convergence is particularly sensitive to the supercell size in the stacking direction. For TBHA, when the supercell size is increased from 16 to 20 along the a direction with the b and c directions fixed, the edge charge percentage increases. When the EWF is generated using a $24 \times 4 \times 4$ fine **k**-point grid, the edge charge fraction drops sharply and about 40% of the total charge is contained within a central volume of 0.1% of the supercell. For HTN, the fraction of edge charge hardly changes with a supercell of $8 \times 6 \times 6$, compared to $8 \times 4 \times 6$, because the b axis is not the main stacking direction. For OBH, whose stacking direction is along c, when the supercell size is changed from $4 \times 10 \times 8$ to $4 \times 8 \times 12$, the edge charge density still decreases despite the shorter length in the b direction.

Finally, we propose a criterion for the supercell convergence for EWF calculations based on the trends observed across different systems. With the finest **k**-point grids used for each crystal, the edge charge increases only slightly when the edge distance is increased from 5% to 25%. The edge charge then rises sharply for edge distances above 25%. Therefore, the supercell size is deemed converged if the edge charge density is less than 5% at an edge distance of 25%. In other words, with the hole position fixed on a molecule in the central sub-cell, more than 95% of the electron density should be contained within a central region of 12.5% of the supercell volume.

2.4. Automated DBA

The DBA method [35] for evaluating the degree of exciton CT character is an extension of the Bader charge partitioning scheme [88] to EWFs with two spatial coordinates. DBA involves performing Bader analysis of electron probability distributions of EWFs calculated with respect to several hole positions, where the probabilities of the hole occupying different sites are determined by Bader analysis of the DFT HOMO of a single molecule. To streamline the DBA procedure, we have developed a new code, dbaAutomator, which performs automated DBA and EWF convergence checks. The dbaAutomator code is written in Python and distributed under an open-source GPL license. Its installation requires only the standard Python libraries ase, pymatgen, and numpy. To perform Bader analysis, dbaAutomator interfaces with a modified version of the Bader Charge Analysis code [88, 89], which is written in Fortran and requires a standard Fortran compiler to install. The dbaAutomator code and documentation can be downloaded from the URL: https://github.com/BLABABA/dbaAutomator. Detailed documentation is also provided in the supporting information.

The workflow of dbaAutomator, illustrated in figure 4, follows the approach suggested in [35]. The Frenkel character, F, is calculated as:

$$F = \sum_{i \in M} W_i \times \sum_{j \in M} P_{e@j}^{h@r_h \in i} \tag{2}$$

where W_i represents the relative probability of the hole being placed within the Bader volume of atom i, which is approximated by the Bader analysis of the DFT HOMO of the molecule M, on which the hole is placed. $P_{e@j}^{h@r_h \in i}$ is the electron density fraction located on atom j of molecule M, which is obtained by Bader analysis of the EWF computed with the hole, h, placed at position r_h within the Bader volume of atom i. Unlike in [35], here only one hole position is sampled in the Bader volume of each atom. This change has been made because sampling multiple hole positions within each probable

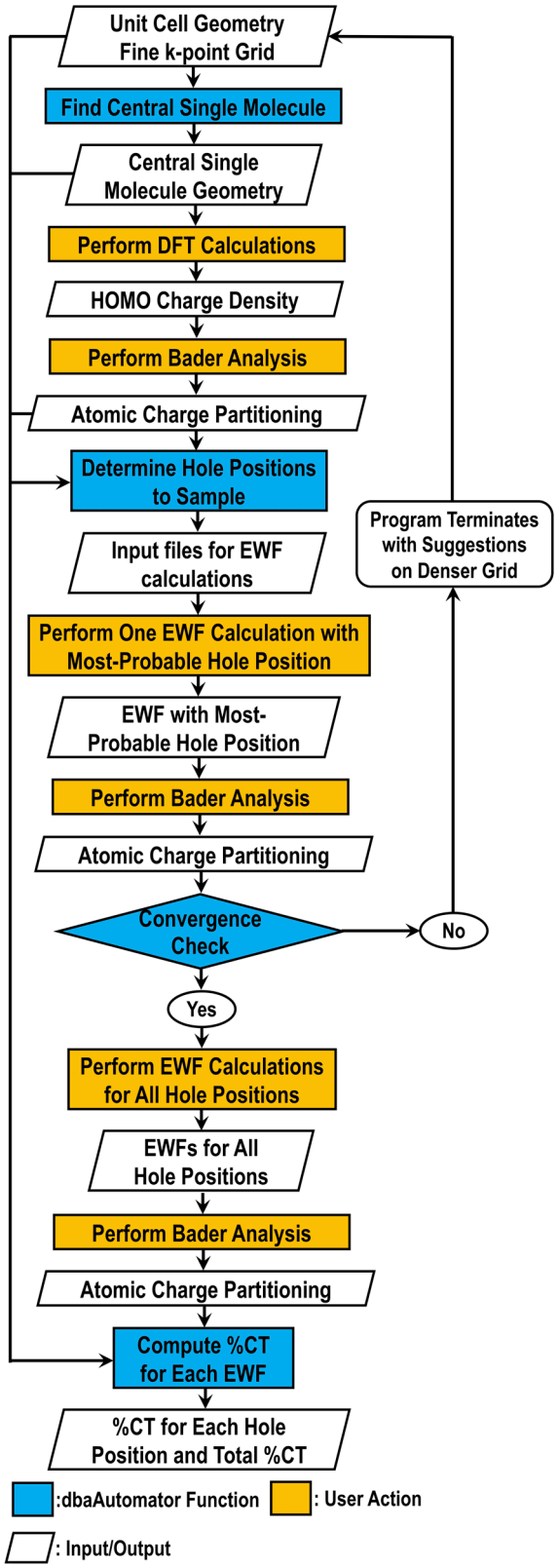

Figure 4. The workflow of dbaAutomator. The parallelograms and rectangles represent inputs/outputs and operations, respectively. Functions performed by dbaAutomator are colored in blue and calculations performed by the user are colored in yellow.

Bader volume demands extensive resources and has a negligible effect on the accuracy of the results. The percentage of CT character (%CT) is then computed as:

$$\%\mathrm{CT} = (1 - F) \cdot 100\%. \tag{3}$$

The workflow of dbaAutomator begins with the unit cell geometry and the fine **k**-point grid used in the mean-field wave-function calculation. Based on this information, dbaAutomator constructs a supercell and identifies and outputs the central molecule M. Next, the user calculates the DFT charge density of the single molecule HOMO in a CUBE format. For this purpose, it may be convenient to use a code that does not impose periodic boundary conditions, such as FHI-aims. Subsequently, the user performs Bader analysis using the Bader Charge Analysis code provided with dbaAutomator. Based on these results, dbaAutomator determines the relative probabilities W_i of the holes occupying different sites on M. Hole positions are sampled next to every atom i of M, whose atomic charge fraction is above 1 %. The user may specify the distance r_h between the center of atom i and the hole h with a default distance of 0.8 Å, as suggested in [35]. BerkeleyGW input files are generated for EWF calculations with all hole positions. To ensure the accuracy of DBA, it is recommended that the user perform an EWF calculation with the most probable hole position, run Bader analysis, and check the convergence of this EWF. The default EWF convergence threshold used in dbaAutomator is an edge charge fraction below 5% of the total electron density at an edge distance of $d = 25\%$, as suggested in section 2.3. If the EWF is deemed unconverged dbaAutomator provides a warning and directs the user to restart the calculation using a denser fine grid. The user should then generates the mean-field wave-function with a denser **k**-point grid. Once this EWF is converged, the user can proceed to calculate the remaining EWFs with the BerkeleyGW inputs provided by dbaAutomator, and perform Bader analysis of the EWFs to compute the electron density fraction $P_{e@j}^{h@r_h \in i}$ for each hole position. Finally, dbaAutomator uses the Bader analysis results from both steps to calculate the total %CT value.

3. Results and discussion

Figure 5 shows the gas phase HOMO-LUMO gap computed with G_0W_0@PBE, as well as the singlet and triplet exciton binding energies and the thermodynamic driving force for SF, $E_S - 2E_T$, of PFAs, compared to acenes and phenylated acenes, classified by their acene backbones. The molecules within each group are presented in the order of increasing size. The effect introduced by the fused pyrene terminals is revealed by comparisons within each group. The HOMO-LUMO gap of TBHA, with two pyrene terminals, is significantly narrower than the gap of anthracene. Similar trends are also observed in the tetracene and pentacene derivatives. For the tetracene series, the HOMO-LUMO gap decreases from 5.02 eV for tetracene to 4.38 eV for rubrene and to 3.82 eV for TBH with one additional pyrene terminal. For the pentacene series, HPP (1,4,6,8,11,13-hexaphenyl-pentacene, CSD reference code: VEBJOC) and DcPP (1,2,3,4,6,8,9,10,11,13-decaphenyl-pentacene, CSD reference code: VEBJAO) yield the lowest HOMO-LUMO gap among all pentacene-based phenylated

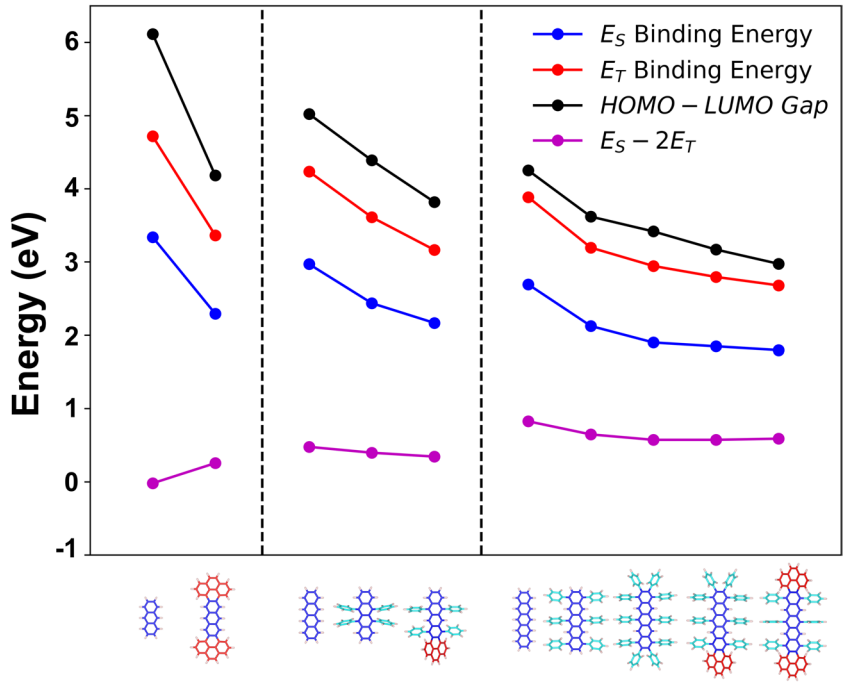

Figure 5. Gas phase HOMO-LUMO gaps, singlet and triplet exciton binding energies, and SF driving force of PFAs, compared to anthracene, tetracene, pentacene, rubrene, HPP and DcPP. Molecular structures are also shown.

acenes, as discussed in [36]. OBH, with one pyrene terminal and eight phenyl side groups, has a smaller gap than the largest phenylated acene, DcPP. HTN, with two pyrene terminals and six phenyl side groups, yields the smallest single molecule gap among all PFAs. The decrease of the fundamental gap with the molecule size may be attributed to the stronger screening provided by the pyrene terminals together with the phenyl side groups. For the same reason, both the singlet and triplet exciton binding energies of phenylated acenes and PFAs monotonically decrease with the molecule size in each series. As a result, the singlet and triplet excitation energies, which are equal to the difference between the fundamental gap and the exciton binding energy, do not change as significantly with the molecule size [36]. Therefore, the pyrene terminals provide stabilization while hardly affecting the thermodynamic driving force for SF, $E_S - 2E_T$.

In the solid state, the fundamental gap narrows compared to the gas phase HOMO-LUMO gap because of the combined effects of band dispersion and polarization [36]. The QP band structures of the PFA crystals, anthracene, and hexacene are shown in figure S1 in the supporting information. The QP band structures of crystalline tetracene and pentacene have been reported in [36]. In agreement with [36], the band dispersion is correlated with the strength of intermolecular interactions. Co-facial interactions between neighboring molecules modulate the electronic coupling between the frontier orbitals, which are located mainly on the acene backbones. The polyacene crystals and TBHA, with no phenyl side groups, have significant band dispersion induced by HB packing or π-stacking. In contrast, the PFA crystals with phenyl side groups, HTN, TBH, and OBH, have flat bands, owing to the absence of co-facial interactions between their backbones.

Figure 6(a) shows the solid-state excitation energies of PFAs compared to the corresponding polyacenes. Due to the errors arising from the various approximations used in GW+BSE calculations, discussed in detail in [35, 36], we restrict the discussion to qualitative trends among materials. In the solid state the singlet and triplet excitation energies do not exhibit monotonic trends with molecule size. The SF driving force of TBHA is smaller than that of anthracene. This makes TBHA a possible candidate for TTA, the reverse process of SF, which may enable harvesting photons with energies below the gap of the absorber in solar cells [90]. TBH and tetracene have very similar singlet and triplet excitation energies. The resulting difference in their SF driving force is around 0.01 eV. For the pentacene derivatives, the singlet excitation energy of OBH is slightly higher than that of pentacene and the triplet excitation energy of HTN is slightly lower than that of pentacene, such that both PFAs have a somewhat higher SF driving force than pentacene. The thermodynamic driving force of HTN is close to that of hexacene.

Figure 6(b) shows the comparison of TBH, OBH, and HTN to tetracene, pentacene, and their phenylated derivatives in terms of their thermodynamic driving force for SF and singlet exciton charge transfer character. ANT and TBHA are not shown in this figure due to their low SF driving force. Overall, the pentacene derivatives have the highest $E_S - 2E_T$ and %CT. The SF driving force of HTN and OBH is somewhat higher than pentacene but lower than the phenylated pentacene derivatives DPP, HPP, and DcPP. All pentacene derivatives have similar %CT. TBH has a very close $E_S - 2E_T$ to that of tetracene, and a higher %CT. Compared to the phenylated tetracene derivatives, the SF driving force of TBH lies between rubrene and DPT. The singlet exciton charge transfer

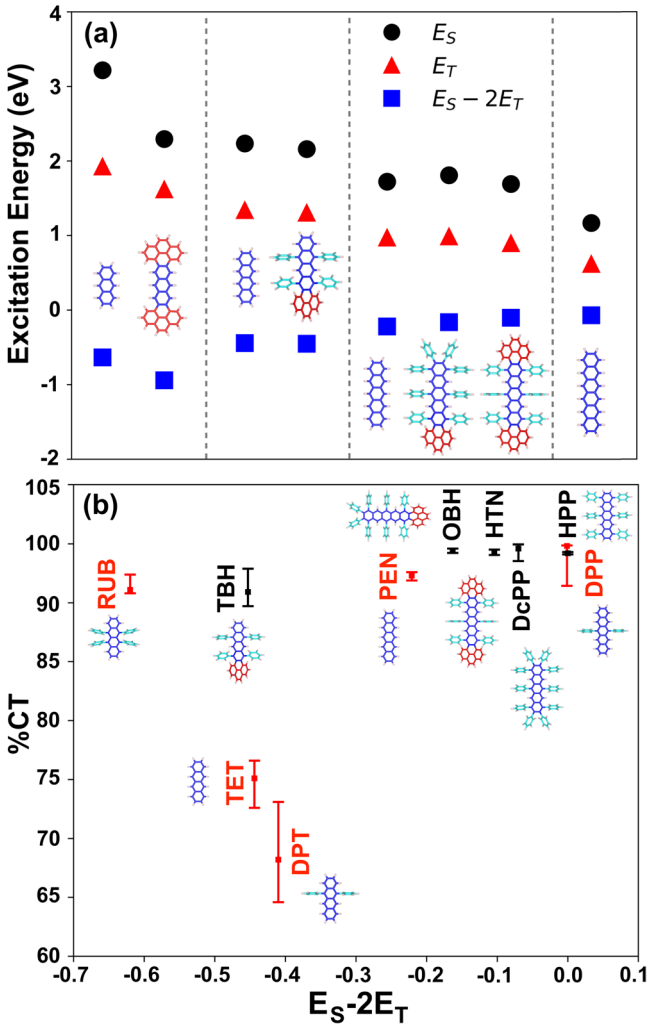

Figure 6. The excitonic properties of crystalline PFAs: (a) Singlet and triplet excitation energies and SF driving force ($E_S - 2E_T$) of PFAs compared to their corresponding acenes. These materials are grouped by their acene backbones and shown in the order of increasing size within each group. (b) Tetracene and pentacene derivatives evaluated in terms of the 2D descriptor, with the thermodynamic driving force for SF ($E_S - 2E_T$) on the x-axis and singlet exciton charge transfer character (%CT) on the y-axis. The squares show the DBA results and the error bars show the minimal and maximal %CT obtained with different hole positions. SF materials observed in experiment are colored in red.

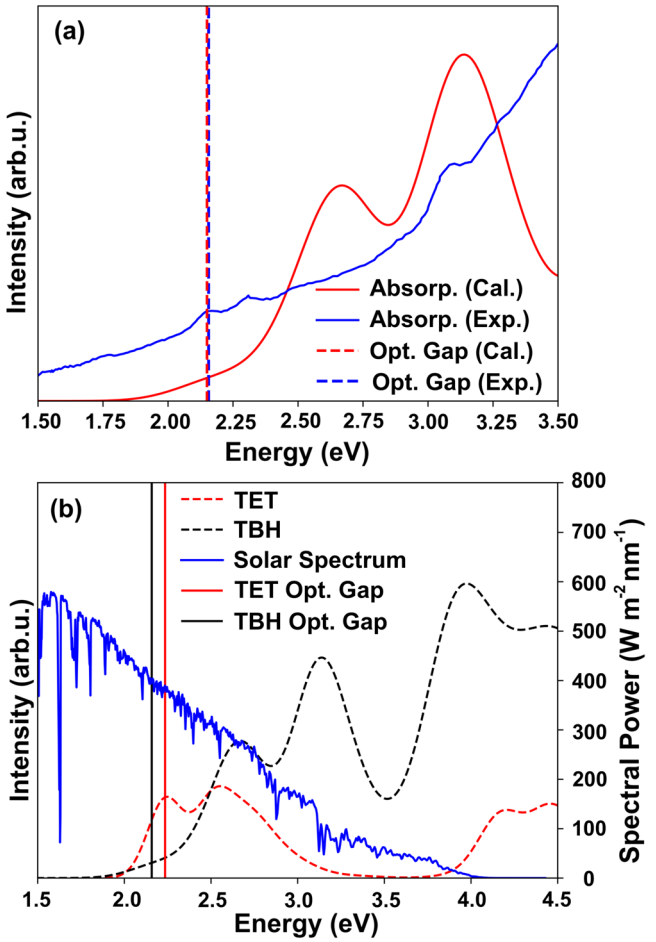

Figure 7. The absorption spectrum of crystalline TBH: (a) comparison between calculated crystal absorption spectrum (solid red line) and experimental thin-film absorption spectrum (solid blue line) of TBH. The dashed red and blue lines indicate the calculated and experimental optical gaps, respectively. The experimental data is from [60]. (b) Comparison between absorption spectra for crystalline tetracene and TBH, shown as dashed red and black lines, respectively. The blue line is the solar spectrum from [91]. The solid black and red lines indicate the optical gaps of TBH and tetracene, respectively.

character of TBH is significantly larger than DPT and close to rubrene. TBH, OBH, and HTN, whose crystal structures are characterized by weak π–π interactions, mostly between the pyrene terminals of neighboring molecules, have a high %CT. This is consistent with the high %CT reported in [36] for phenylated acenes with weak co-facial interactions.

Finally, the G_0W_0 + BSE@PBE absorption spectra of PFAs are compared to the corresponding acenes to evaluate their suitability for solar cell modules. Figure 7(a) shows the experimental [62] and calculated absorption spectra of TBH. The experimental spectrum was measured for a thin film with no information regarding the direction of light polarization with respect to the crystal axes. Therefore, the calculated absorption spectrum is a summation over the spectra obtained with polarization along the a, b, and c directions. The calculated optical gap is in close agreement with experiment. However, the spectral shape does not match the experiment as closely. This could be attributed to possible anisotropy of the thin film. In figure 7(b), the absorption spectrum of TBH is compared to tetracene. The solar spectrum [91] is also shown. Crystalline tetracene displays strong absorption ranging from 2.2 eV to 3.0 eV. In comparison, crystalline TBH presents a broader absorption range, from around 2.2 eV to 4.0 eV. Beyond 4.0 eV the solar spectrum diminishes, indicating that absorption in this range would not contribute to the total PCE of a solar cell. Hence, TBH may exhibit comparable performance to tetracene in terms of light absorption.

Figure S2 in the supporting information shows the computed absorption spectra of HTN and OBH compared to pentacene. Pentacene absorbs strongly in the range of 1.7 eV to about 2.5 eV. The HTN and OBH crystals show absorption

peaks in the range of 2.7 eV to 3.3 eV, where there is a gap in the absorption spectrum of pentacene. Therefore, HTN or OBH could serve as complementary absorbers to pentacene.

4. Conclusions

We have examined the excitonic properties of pyrene-fused acene derivatives using many-body perturbation theory within the GW+BSE formalism. We have proposed a criterion for determining whether EWFs are converged with respect to the fine **k**-point grid used in the BerkeleyGW code, which corresponds to the supercell size. If the hole position is fixed at a high-probability site on a molecule in the central sub-cell, more than 95% of the total electron density should be contained within a volume fraction of 12.5% in the central region of the supercell. A new open-source Python program, dbaAutomator, has been developed to perform convergence checks and streamline the DBA of EWFs.

We find that the excitonic properties of PFAs are comparable to the corresponding acenes and phenylated acene derivatives. TBHA has a lower SF driving force than anthracene. Therefore, it could be a possible candidate for triplet–triplet annihilation. OBH and HTN have somewhat higher SF driving forces and singlet exciton CT characters than pentacene. They could serve as complementary absorbers to pentacene because they absorb light in the energy range where pentacene exhibits an absorption gap. TBH has a similar SF driving force to tetracene and a higher degree of singlet exciton CT character. In addition, TBH absorbs light in a similar range to tetracene and could be paired with crystalline silicon [17]. Hence, it could be a promising candidate to replace tetracene. In conclusion, pyrene-fused pentacene and tetracene derivatives could be prospective SF candidates with enhanced stability.

Acknowledgments

Work at CMU was funded by the Charles E Kaufman Foundation through Grant KA2017-91789 and by the National Science Foundation (NSF) Division of Materials Research through Grant DMR-1844484. We thank Diana Qiu from Yale University, Felippe de Jornada from Stanford University and Mauro Del Ben from Lawrence Berkeley National Laboratory for their helpful discussions on the calculations and convergence of EWFs. This work used computing resources provided by the Argonne Leadership Computing Facility (ALCF), which is a DOE Office of Science User Facility supported under contract no. DE-AC02-06CH11357 and the National Energy Research Scientific Computing Center (NERSC), a DOE Office of Science User Facility supported by the Office of Science of the US Department of Energy under contract no. DE-AC02-05CH11231.

ORCID iDs

Noa Marom https://orcid.org/0000-0002-1508-1312

References

[1] Smith M and Michl J 2010 Singlet fission *Chem. Rev.* **110** 6891–936
[2] Smith M B and Michl J 2013 Recent advances in singlet fission *Annu. Rev. Phys. Chem.* **64** 361–86
[3] Monahan N and Zhu X-Y 2015 Charge transfer-mediated singlet fission *Annu. Rev. Phys. Chem.* **66** 601–18
[4] Rao A and Friend R H 2017 Harnessing singlet exciton fission to break the Shockley–Queisser limit *Nat. Rev. Mater.* **2** 1–12
[5] Casanova D 2018 Theoretical modeling of singlet fission *Chem. Rev.* **118** 7164–207
[6] Chan W-L, Ligges M, Jailaubekov A, Kaake L, Miaja-Avila L and Zhu X-Y 2011 Observing the multiexciton state in singlet fission and ensuing ultrafast multielectron transfer *Science* **334** 1541–5
[7] Hanna M C and Nozik A J 2006 Solar conversion efficiency of photovoltaic and photoelectrolysis cells with carrier multiplication absorbers *J. Appl. Phys.* **100** 074510
[8] Shockley W and Queisser H J 1961 Detailed balance limit of efficiency of p-n junction solar cells *J. Appl. Phys.* **32** 510–9
[9] Congreve D N, Lee J, Thompson N J, Hontz E, Yost S R, Reusswig P D, Bahlke M E, Reineke S, Van Voorhis T and Baldo M A 2013 External quantum efficiency above 100% in a singlet-exciton-fission-based organic photovoltaic cell *Science* **340** 334–7
[10] Wu T C, Thompson N J, Congreve D N, Hontz E, Yost S R, Van Voorhis T and Baldo M A 2014 Singlet fission efficiency in tetracene-based organic solar cells *Appl. Phys. Lett.* **104** 193901
[11] Ehrler B, Walker B J, Böhm M L, Wilson M W B, Vaynzof Y, Friend R H and Greenham N C 2012 *In situ* measurement of exciton energy in hybrid singlet-fission solar cells *Nat. Commun.* **3** 1019
[12] Thompson N J *et al* 2014 Energy harvesting of non-emissive triplet excitons in tetracene by emissive PbS nanocrystals *Nat. Mater.* **13** 1039–43
[13] Lee J, Jadhav P, Reusswig P D, Yost S R, Thompson N J, Congreve D N, Hontz E, Van Voorhis T and Baldo M A 2013 Singlet exciton fission photovoltaics *Acc. Chem. Res.* **46** 1300–11
[14] Ehrler B, Wilson M W B, Rao A, Friend R H and Greenham N C 2012 Singlet exciton fission-sensitized infrared quantum dot solar cells *Nano Lett.* **12** 1053–7
[15] Yang L, Tabachnyk M, Bayliss S L, Böhm M L, Broch K, Greenham N C, Friend R H and Ehrler B 2015 Solution-processable singlet fission photovoltaic devices *Nano Lett.* **15** 354–8
[16] Pazos-Outón L M, Lee J M, Futscher M H, Kirch A, Tabachnyk M, Friend R H and Ehrler B 2017 A silicon-singlet fission tandem solar cell exceeding 100% external quantum efficiency with high spectral stability *ACS Energy Lett.* **2** 476–80
[17] Einzinger M *et al* 2019 Sensitization of silicon by singlet exciton fission in tetracene *Nature* **571** 90–4
[18] Davis N J L K, Allardice J R, Xiao J, Petty A J, Greenham N C, Anthony J E and Rao A 2018 Singlet fission and triplet transfer to PbS quantum dots in TIPS-tetracene carboxylic acid ligands *J. Phys. Chem. Lett.* **9** 1454–60
[19] Schrauben J N, Zhao Y, Mercado C, Dron P I, Ryerson J L, Michl J, Zhu K and Johnson J C 2015 Photocurrent enhanced by singlet fission in a dye-sensitized solar cell *ACS Appl. Mater. Interfaces* **7** 2286–93
[20] Wilson M W B, Rao A, Ehrler B and Friend R H 2013 Singlet exciton fission in polycrystalline pentacene: from photophysics toward devices *Acc. Chem. Res.* **46** 1330–8

[21] Dexter D L 1979 Two ideas on energy transfer phenomena: ion-pair effects involving the OH stretching mode, and sensitization of photovoltaic cells *J. Lumin.* **18–19** 779–84

[22] Havlas Z, Wen J and Michl J 2015 Singlet fission: towards efficient solar cells *AIP Conf. Proc.* **1702** 090017

[23] Schnedermann C *et al* 2019 A molecular movie of ultrafast singlet fission *Nat. Commun.* **10** 4207

[24] Schröder F A Y N, Turban D H P, Musser A J, Hine N D M and Chin A W 2019 Tensor network simulation of multi-environmental open quantum dynamics via machine learning and entanglement renormalisation *Nat. Commun.* **10** 1–10

[25] Lukman S, Chen K, Hodgkiss J M, Turban D H P, Hine N D M, Dong S, Wu J, Greenham N C and Musser A J 2016 Tuning the role of charge-transfer states in intramolecular singlet exciton fission through side-group engineering *Nat. Commun.* **7** 1–13

[26] Alvertis A M, Lukman S, Hele T J H, Fuemmeler E G, Feng J, Wu J, Greenham N C, Chin A W and Musser A J 2019 Switching between coherent and incoherent singlet fission via solvent-induced symmetry breaking *J. Am. Chem. Soc.* **141** 17558–70

[27] Johnson J C, Nozik A J and Michl J 2013 The role of chromophore coupling in singlet fission *Acc. Chem. Res.* **46** 1290–9

[28] Chan W L, Ligges M and Zhu X Y 2012 The energy barrier in singlet fission can be overcome through coherent coupling and entropic gain *Nat. Chem.* **4** 840–5

[29] Tamura H, Huix-Rotllant M, Burghardt I, Olivier Y and Beljonne D 2015 First-principles quantum dynamics of singlet fission: coherent versus thermally activated mechanisms governed by molecular π stacking *Phys. Rev. Lett.* **115** 1–5

[30] Buchanan E A, Kaleta J, Wen J, Lapidus S H, Císařová I, Havlas Z, Johnson J C and Michl J 2019 Molecular packing and singlet fission: the parent and three fluorinated 1,3-diphenylisobenzofurans *J. Phys. Chem. Lett.* **10** 1947–53

[31] Walker B J, Musser A J, Beljonne D and Friend R H 2013 Singlet exciton fission in solution *Nat. Chem.* **5** 1019–24

[32] Yost S R *et al* 2014 A transferable model for singlet-fission kinetics *Nat. Chem.* **6** 492–7

[33] Sharifzadeh S, Darancet P, Kronik L and Neaton J B 2013 Low-energy charge-transfer excitons in organic solids from first-principles: the case of pentacene *J. Phys. Chem. Lett.* **4** 2197–201

[34] Beljonne D, Yamagata H, Brédas J L, Spano F C and Olivier Y 2013 Charge-transfer excitations steer the davydov splitting and mediate singlet exciton fission in pentacene *Phys. Rev. Lett.* **110** 226402

[35] Wang X, Liu X, Cook C, Schatschneider B and Marom N 2018 On the possibility of singlet fission in crystalline quaterrylene *J. Chem. Phys.* **148** 184101

[36] Wang X, Liu X, Tom R, Cook C, Schatschneider B and Marom N 2019 Phenylated acene derivatives as candidates for intermolecular singlet fission *J. Phys. Chem.* C **123** 5890–9

[37] Berkelbach T C, Hybertsen M S and Reichman D R 2013 Microscopic theory of singlet exciton fission. I. General formulation *J. Chem. Phys.* **138** 114102

[38] Sharifzadeh S, Wong C Y, Wu H, Cotts B L, Kronik L, Ginsberg N S and Neaton J B 2015 Relating the physical structure and optoelectronic function of crystalline TIPS-pentacene *Adv. Funct. Mater.* **25** 2038–46

[39] Zeng T, Hoffmann R and Ananth N 2014 The low-lying electronic states of pentacene and their roles in singlet fission *J. Am. Chem. Soc.* **136** 5755–64

[40] Berkelbach T C, Hybertsen M S and Reichman D R 2014 Microscopic theory of singlet exciton fission. III. Crystalline pentacene *J. Chem. Phys.* **141** 74705

[41] Chan W L, Berkelbach T C, Provorse M R, Monahan N R, Tritsch J R, Hybertsen M S, Reichman D R, Gao J and Zhu X Y 2013 The quantum coherent mechanism for singlet fission: experiment and theory *Acc. Chem. Res.* **46** 1321–9

[42] Feng X, Kolomeisky A B and Krylov A I 2014 Dissecting the effect of morphology on the rates of singlet fission: insights from theory *J. Phys. Chem.* C **118** 19608–17

[43] Wang X, Garcia T, Monaco S, Schatschneider B and Marom N 2016 Effect of crystal packing on the excitonic properties of rubrene polymorphs *CrystEngComm* **18** 7353–62

[44] Wang L, Olivier Y, Prezhdo O V and Beljonne D 2014 Maximizing singlet fission by intermolecular packing *J. Phys. Chem. Lett.* **5** 3345–53

[45] Jundt C, Klein G, Sipp B, Le Moigne J, Joucla M and Villaeys A A 1995 Exciton dynamics in pentacene thin films studied by pump-probe spectroscopy *Chem. Phys. Lett.* **241** 84–8

[46] Wilson M W B, Rao A, Clark J, Kumar R S S, Brida D, Cerullo G and Friend R H 2011 Ultrafast dynamics of exciton fission in polycrystalline pentacene *J. Am. Chem. Soc.* **133** 11830–3

[47] Hestand N J, Yamagata H, Xu B, Sun D, Zhong Y, Harutyunyan A R, Chen G, Dai H L, Rao Y and Spano F C 2015 Polarized absorption in crystalline pentacene: theory versus experiment *J. Phys. Chem.* C **119** 22137–47

[48] Thorsmølle V K, Averitt R D, Demsar J, Smith D L, Tretiak S, Martin R L, Chi X, Crone B K, Ramirez A P and Taylor A J 2009 Morphology effectively controls singlet-triplet exciton relaxation and charge transport in organic semiconductors *Phys. Rev. Lett.* **102** 017401

[49] Rangel T, Berland K, Sharifzadeh S, Brown-Altvater F, Lee K, Hyldgaard P, Kronik L and Neaton J B 2016 Structural and excited-state properties of oligoacene crystals from first principles *Phys. Rev.* B **93** 1–16

[50] Bree B A and Lyons L E 1960 The intensity of ultraviolet-light absorption by monocrystals. Part IV. Absorption by naphthacenc of plane-polarized light *J. Chem. Soc.* **22** 5206–12

[51] Lim S H, Bjorklund T G, Spano F C and Bardeen C J 2004 Exciton delocalization and superradiance in tetracene thin films and nanoaggregates *Phys. Rev. Lett.* **92** 107402

[52] Ye Q and Chi C 2014 Recent highlights and perspectives on acene based molecules and materials *Chem. Mater.* **26** 4046–56

[53] Jadhav P J *et al* 2012 Triplet exciton dissociation in singlet exciton fission photovoltaics *Adv. Mater.* **24** 6169–74

[54] Roberts S T, McAnally R E, Mastron J N, Webber D H, Whited M T, Brutchey R L, Thompson M E and Bradforth S E 2012 Efficient singlet fission discovered in a disordered acene film *J. Am. Chem. Soc.* **134** 6388–400

[55] Wolf E A, Finton D M, Zoutenbier V and Biaggio I 2018 Quantum beats of a multiexciton state in rubrene single crystals *Appl. Phys. Lett.* **112** 83301

[56] Ma L, Zhang K, Kloc C, Sun H, Michel-Beyerle M E and Gurzadyan G G 2012 Singlet fission in rubrene single crystal: direct observation by femtosecond pump-probe spectroscopy *Phys. Chem. Chem. Phys.* **14** 8307–12

[57] Pal A K, Bhattacharyya K and Datta A 2019 Remote functionalization through symmetric or asymmetric substitutions control the pathway of intermolecular singlet fission *J. Chem. Theory Comput.* **15** 5014–23

[58] Bhattacharyya K and Datta A 2017 Polymorphism controlled singlet fission in tips-anthracene: role of stacking orientation *J. Phys. Chem.* C **121** 1412–20

[59] Chen Y, Shen L and Li X 2014 Effects of heteroatoms of tetracene and pentacene derivatives on their stability and singlet fission *J. Phys. Chem.* A **118** 5700–8

[60] Xiao J, Liu S, Liu Y, Ji L, Liu X, Zhang H, Sun X and Zhang Q 2012 Synthesis, structure, and physical properties of 5,7,14,16-tetraphenyl-8:9, 12:13-bisbenzo-hexatwistacene *Chem. Asian J.* **7** 561–4

[61] Xiao J *et al* 2012 Synthesis and structure characterization of a stable nonatwistacene *Angew. Chem., Int. Ed. Engl.* **51** 6094–8

[62] Xiao J, Malliakas C D, Liu Y, Zhou F, Li G, Su H, Kanatzidis M G, Wudl F and Zhang Q 2012 'Clean reaction' strategy to approach a stable, green heptatwistacene containing a single terminal pyrene unit *Chem. Asian J.* **7** 672–5

[63] Li J, Chen S, Wang Z and Zhang Q 2016 Pyrene-fused acenes and azaacenes: synthesis and applications *Chem. Rec.* **16** 1518–30

[64] Mason R 1964 The crystallography of anthracene at 95 K and 290 K *Acta Crystallogr.* **17** 547–55

[65] Holmes D, Kumaraswamy S, Matzger A J and Vollhardt K P C 1999 On the nature of nonplanarity in the [N]Phenylenes *Chem. Eur. J.* **5** 3399–412

[66] Campbell R B, Robertson J M and Trotter J 1962 The crystal structure of hexacene, and a revision of the crystallographic data for tetracene and pentacene *Acta Crystallogr.* **15** 289–90

[67] Watanabe M, Chang Y J, Liu S W, Chao T H, Goto K, Islam M M, Yuan C H, Tao Y T, Shinmyozu T and Chow T J 2012 The synthesis, crystal structure and charge-transport properties of hexacene *Nat. Chem.* **4** 574–8

[68] Ferguson G and Parvez M 1979 Tetrabenzo[*de*,*no*,*st*,c_1d_1] heptacene *Acta Crystallogr.* **35** 2419–21

[69] Hammouri M, Garcia T M, Cook C, Monaco S, Jezowski S, Marom N and Schatschneider B 2018 High-throughput pressure-dependent density functional theory investigation of herringbone polycyclic aromatic hydrocarbons: part 2. Pressure-dependent electronic properties *J. Phys. Chem.* C **122** 23828–44

[70] Perdew J P, Burke K and Ernzerhof M 1996 Generalized gradient approximation made simple *Phys. Rev. Lett.* **77** 3865–8

[71] Tkatchenko A and Scheffler M 2009 Accurate molecular Van Der Waals interactions from ground-state electron density and free-atom reference data *Phys. Rev. Lett.* **102** 073005

[72] Blum V, Gehrke R, Hanke F, Havu P, Havu V, Ren X, Reuter K and Scheffler M 2009 *Ab initio* molecular simulations with numeric atom-centered orbitals *Comput. Phys. Commun.* **180** 2175–96

[73] Ren X, Rinke P, Blum V, Wieferink J, Tkatchenko A, Sanfilippo A, Reuter K and Scheffler M 2012 Resolution-of-identity approach to Hartree–Fock, hybrid density functionals, RPA, MP2 and GW with numeric atom-centered orbital basis functions *New J. Phys.* **14** 053020

[74] Havu V, Blum V, Havu P and Scheffler M 2009 Efficient O(N) integration for all-electron electronic structure calculation using numeric basis functions *J. Comput. Phys.* **228** 8367–79

[75] Clark S J, Segall M D, Pickard C J, Hasnip P J, Probert M I J, Refson K and Payne M C 2005 First principles methods using CASTEP *Z. Kristallogr.* **220** 567–70

[76] Liu C, Kloppenburg J, Ren X, Appel H, Kanai Y and Blum V 2019 *Ab initio* Bethe–Salpeter equation approach to neutral excitations in molecules with numeric atom-centered orbitals (arXiv:1908.01431)

[77] Knight J W, Wang X, Gallandi L, Dolgounitcheva O, Ren X, Ortiz J V, Rinke P, Körzdörfer T and Marom N 2016 Accurate ionization potentials and electron affinities of acceptor molecules III: A benchmark of GW methods *J. Chem. Theory Comput.* **12** 615–26

[78] Jacquemin D, Duchemin I and Blase X 2015 Benchmarking the Bethe–Salpeter formalism on a standard organic molecular set *J. Chem. Theory Comput.* **11** 3290–304

[79] Deslippe J, Samsonidze G, Strubbe D A, Jain M, Cohen M L and Louie S G 2012 BerkeleyGW: a massively parallel computer package for the calculation of the quasiparticle and optical properties of materials and nanostructures *Comput. Phys. Commun.* **183** 1269–89

[80] Sharifzadeh S 2018 Many-body perturbation theory for understanding optical excitations in organic molecules and solids *J. Phys.: Condens. Matter* **30** 153002

[81] Musser A J, Liebel M, Schnedermann C, Wende T, Kehoe T B, Rao A and Kukura P 2015 Evidence for conical intersection dynamics mediating ultrafast singlet exciton fission *Nat. Phys.* **11** 352–7

[82] Monserrat B, Engel E A and Needs R J 2015 Giant electron–phonon interactions in molecular crystals and the importance of nonquadratic coupling *Phys. Rev.* B **92** 1–6

[83] Hybertsen M S and Louie S G 1986 Electron correlation in semiconductors and insulators: band gaps and quasiparticle energies *Phys. Rev.* B **34** 5390–413

[84] Rohlfing M and Louie S G 2000 Electron-hole excitations and optical spectra from first principles *Phys. Rev.* B **62** 4927–44

[85] Giannozzi P *et al* 2009 QUANTUM ESPRESSO: a modular and open-source software project for quantum simulations of materials *J. Phys.: Condens. Matter* **21** 1–19

[86] Troullier N and Martins J L 1991 Efficient pseudopotentials for plane-wave calculations *Phys. Rev.* B **43** 1993–2006

[87] Deslippe J, Samsonidze G, Jain M, Cohen M L and Louie S G 2013 Coulomb-hole summations and energies for GW calculations with limited number of empty orbitals: a modified static remainder approach *Phys. Rev.* B **87** 165124

[88] Tang W, Sanville E and Henkelman G 2009 A grid-based Bader analysis algorithm without lattice bias *J. Phys.: Condens. Matter* **21** 084204

[89] Yu M and Trinkle D R 2011 Accurate and efficient algorithm for Bader charge integration *J. Chem. Phys.* **134** 1–8

[90] Schulze T F and Schmidt T W 2015 Photochemical upconversion: present status and prospects for its application to solar energy conversion *Energy Environ. Sci.* **8** 103–25

[91] Gueymard C A 2001 Parameterized transmittance model for direct beam and circumsolar spectral irradiance *Sol. Energy* **71** 325–46